Sculpting liquid crystal skyrmions with external flows

Rodrigo C. V. Coelho [⬤],[1,2,*] Hanqing Zhao,[3] Mykola Tasinkevych [⬤],[1,2,4,5,†] Ivan I. Smalyukh,[3,6,7,5,‡]
and Margarida M. Telo da Gama [⬤][1,2]

[1]*Centro de Física Teórica e Computacional, Faculdade de Ciências, Universidade de Lisboa, 1749-016 Lisboa, Portugal*
[2]*Departamento de Física, Faculdade de Ciências, Universidade de Lisboa, P-1749-016 Lisboa, Portugal*
[3]*Department of Physics and Soft Materials Research Center, University of Colorado Boulder, Colorado 80309, USA*
[4]*SOFT Group, School of Science and Technology, Nottingham Trent University, Clifton Lane, Nottingham NG11 8NS, United Kingdom*
[5]*International Institute for Sustainability with Knotted Chiral Meta Matter, Hiroshima University, Higashihiroshima 739-8511, Japan*
[6]*Department of Electrical, Computer, and Energy Engineering and Materials Science and Engineering Program,
University of Colorado, Boulder, Colorado 80309, USA*
[7]*Renewable and Sustainable Energy Institute, National Renewable Energy Laboratory and University of Colorado,
Boulder, Colorado 80309, USA*

We investigate, using experiments and numerical simulations, the distortions and the alignment of skyrmions in liquid crystal under external flows for a range of average flow velocities. The simulations are based on the Landau-de Gennes Q tensor theory both for isolated as well as for systems with many skyrmions. We found striking flow-driven elongation of an isolated skyrmion and flow alignment of skyrmions in the many-skyrmion system, both of which are also observed in the experiments. In the simulations, particular attention was given to the dissipation rate and to the various dissipation channels for a single skyrmion under external flow. This analysis provides insight on the observed scaling regime of the elongation of isolated flowing skyrmions and revealed a surprising plastic response at very short times, which may be relevant in applications based on the alignment of soft structures such as liquid crystal skyrmions.

I. INTRODUCTION

Liquid crystals (LCs) are unique soft materials that exhibit facile responses to external electric and magnetic fields. Additionally, the LC molecular orientation field, the director, can be easily distorted by anchoring at solid boundaries. These properties of LCs are the cornerstone of modern display technologies [1]. In LC displays the director field undergoes continuous transitions between distinct topologically trivial configurations, i.e., configurations that can be morphed into a uniform structure continuously. Topological point or line defects may be spontaneously nucleated but these singular configurations are usually short-lived transient structures.

Cholesteric LCs exhibit a particularly large variety of director structures under various conditions of surface confinement and applied external fields, which throughout the history were classified mainly based on their appearance under a polarizing optical microscope [2]. Among these structures are various cholesteric fingers and bubbles, where the

former are linear and the latter are circular-looking localized domains of the director field [3–27]. While some of these structures are topologically trivial (e.g., the so-called cholesteric fingers of the 1st kind can be smoothly morphed to the uniform/trivial state), the other ones were later shown to have topologically nontrivial structures. For example, for weak perpendicular surface boundary conditions the so-called baby skyrmions were shown to be topologically nontrivial two dimensional (2D) translationally invariant structures, which are classified in terms of elements of the 2nd homotopy group of the order parameter space of nonpolar unit vectors [28]. The director configuration of the baby skyrmion exhibits uniform twisting by 180° from its center in all radial directions [29].

Under strong perpendicular boundary conditions, the skyrmion tubes terminate on point defects, which are also elements of the second homotopy group, and which allow embedding of the skyrmion tube in a uniform/trivial background director field in 3D. These configurations were called "torons" and their midsample plane configuration corresponds to that of the 2D baby skyrmion. Torons were found experimentally in chiral LCs [30], but later also observed in noncentrosymmetric magnets [31,32] and other systems, where the name coined within the LC field was also adopted and is now commonly used [33–35].

Interestingly, cholesteric fingers of the second (CF2) type are also skyrmion tubes laterally stretched and terminating on point defects. Therefore, CF2s are expected to be homeomorphic to torons, albeit they have a very different appearance under the polarizing optical microscope. The torons and CF2s

*rcvcoelho@fc.ul.pt
†mykola.tasinkevych@ntu.ac.uk
‡ivan.smalyukh@colorado.edu

are effectively two different geometric embodiments of the same topological object, much like a coffee mug and a dough-nut have the same surface topology, and one would, thus, expect to being able to morph one into another. Such home-omorphic transformation was indeed demonstrated by Sohn *et al.* using laser tweezers [36], but the question arises if topology-preserving morphing can be also realized by other physical stimuli [37–40], including fluid flows.

Despite the extensive body of research on LC solitons, their interaction with externally imposed material flow fields remains poorly understood. In our recent paper [41] we reported a numerical study, based on the Ericksen-Leslie nematohydro-dynamics, of the effect of external flows on the structures and dynamics of LC skyrmions. We found a configurational transi-tion driven by the flow, from skyrmionic distortions along the flow in weak flows to skyrmionic distortions in the direction perpendicular to the flow in strong flows.

Here, we extend that study and address explicitly the re-versibility of the flow induced skyrmionic distortions. We reformulate the problem in terms of the Landau-de Gennes Q tensor theory and compare different contributions to the dissi-pated energy. This analysis provides insight on the distortions observed in skyrmions under flow and reveals the mechanisms of their plastic response, which may be key in applications based on the elongation and alignment of soft structures such as liquid crystal skyrmions.

Numerical results for the flow-induced elongation of a baby skyrmion agree qualitatively with experimental observa-tions. We also report on the collective behavior of skyrmions driven by external flows observed both in the simulations and in experiments. The most significant many-body effects are the hindering of skyrmionic elongations by the presence of other skyrmions and the collective skyrmion alignment by the external flow.

In Sec. II, we provide a description of the numerical meth-ods used to solve the dynamics of the Landau-de Gennes Q tensor theory under mass flow, i.e., the Beris-Edwards, the continuity, and the Navier-Stokes equations, and describe the experimental system and methods. In Sec. III, we report numerical results for the distortion of an isolated skyrmion, and compare them with the experimental observations. We also describe the collective behavior of flowing skyrmions observed numerically and experimentally, where the effects of strong interactions are revealed. Finally, in Sec. IV, we discuss the results and summarize the conclusions.

II. METHODS

A. Beris-Edwards model for flowing skyrmions

The model used to describe the liquid crystal skyrmions under mass flow is based on the Landau-de Gennes Q tensor theory of nematics [42,43]. For uniaxial ordered phases, the tensor order parameter is $Q_{\alpha\beta} = S(n_\alpha n_\beta - \delta_{\alpha\beta}/3)$, where S is the scalar order parameter, which equals to zero in the isotropic phase and unity in phases with perfect alignment, and n_α is the director field. The free energy of the liquid crystal is $\mathcal{F} = \int_V d^3r \, f$, where the free energy density f has three contributions:

$$f_b = a\,Q_{\alpha\beta}{}^2 - b\,(Q_{\alpha\beta}Q_{\beta\gamma}Q_{\gamma\alpha}) + c\,Q_{\alpha\beta}{}^4, \quad (1)$$

$$f_{el} = \frac{L_1}{2}(\partial_\gamma Q_{\alpha\beta})^2 + \frac{L_2}{2}\partial_\epsilon Q_{\nu\epsilon}\partial_\gamma Q_{\nu\gamma} + \frac{4\pi L_1}{p}\varepsilon_{\alpha\beta\gamma}Q_{\alpha\epsilon}\partial_\beta Q_{\gamma\epsilon}, \quad (2)$$

$$f_w = \frac{W}{2}\left(Q_{\alpha\beta} - Q_{\alpha\beta}^0\right)^2. \quad (3)$$

The first is the bulk free energy and a, b, and c are positive material constants. The second is the elastic free energy with two elastic constants L_1 and L_2 [44,45] and p is the equilib-rium cholesteric pitch. The last contribution arises from the anchoring at the confining surfaces. As the simulations are effectively 2D, one needs to apply this anchoring everywhere (as a bulk term) to stabilize the skyrmions [41,46,47]. The parameter W controls the anchoring strength.

The dynamics is governed by the Beris-Edwards, the con-tinuity and the Navier-Stokes [48] equations:

$$\partial_t Q_{\alpha\beta} + u_\gamma \partial_\gamma Q_{\alpha\beta} - S_{\alpha\beta} = \Gamma H_{\alpha\beta}, \quad (4)$$

$$\partial_\beta u_\beta = 0, \quad (5)$$

$$\rho\partial_t u_\alpha + \rho u_\beta\partial_\beta u_\alpha = -\chi u_\alpha + \partial_\beta\big[2\eta A_{\alpha\beta} + \sigma_{\alpha\beta}^{\mathrm{n}} + \rho f_\alpha\big], \quad (6)$$

where ρ is the liquid crystal density and Γ is the system dependent rotational diffusivity. Equation (4) describes the time evolution of the order parameter $Q_{\alpha\beta}$, which depends on the velocity field u_α. The dynamics of the velocity field is given by Eq. (6), which depends on $Q_{\alpha\beta}$. The first term on the right-hand side of Eq. (6) stands for the effective friction at the surfaces [41]. For Poiseuille flow of a fluid with absolute vis-cosity $\eta = \rho\nu$ between two surfaces separated by a distance L, the friction coefficient in 2D that yields the same average ve-locity of the 3D flow is $\chi = 12\eta/L^2$, where ν is the kinematic viscosity. The fluid moves driven by an external force f_α. In the equations above, the shear rate and the vorticity are given by $A_{\alpha\beta} = (\partial_\alpha u_\beta + \partial_\beta u_\alpha)/2$ and $W_{\alpha\beta} = (\partial_\beta u_\alpha - \partial_\alpha u_\beta)/2$ and the corotational term reads

$$S_{\alpha\beta} = (\xi A_{\alpha\gamma} + W_{\alpha\gamma})\left(Q_{\beta\gamma} + \frac{\delta_{\beta\gamma}}{3}\right)$$
$$+ \left(Q_{\alpha\gamma} + \frac{\delta_{\alpha\gamma}}{3}\right)(\xi A_{\gamma\beta} - W_{\gamma\beta})$$
$$- 2\xi\left(Q_{\alpha\beta} + \frac{\delta_{\alpha\beta}}{3}\right)(Q_{\gamma\epsilon}\partial_\gamma u_\epsilon), \quad (7)$$

where ξ is the flow aligning parameter. The molecular field is

$$H_{\alpha\beta} = -\frac{\delta\mathcal{F}}{\delta Q_{\alpha\beta}} + \frac{\delta_{\alpha\beta}}{3}\mathrm{Tr}\left(\frac{\delta\mathcal{F}}{\delta Q_{\gamma\epsilon}}\right), \quad (8)$$

and the nematic stress tensor is given by

$$\sigma_{\alpha\beta}^{\mathrm{n}} = -P_0\delta_{\alpha\beta} + 2\xi\left(Q_{\alpha\beta} + \frac{\delta_{\alpha\beta}}{3}\right)Q_{\gamma\epsilon}H_{\gamma\epsilon}$$
$$- \xi H_{\alpha\gamma}\left(Q_{\gamma\beta} + \frac{\delta_{\gamma\beta}}{3}\right) - \xi\left(Q_{\alpha\gamma} + \frac{\delta_{\alpha\gamma}}{3}\right)H_{\gamma\beta}$$
$$- \frac{\delta\mathcal{F}}{\delta(\partial_\beta Q_{\gamma\nu})}\partial_\alpha Q_{\gamma\nu} + Q_{\alpha\gamma}H_{\gamma\beta} - H_{\alpha\gamma}Q_{\gamma\beta}, \quad (9)$$

with P_0 the hydrostatic pressure. Although the scalar order parameter S does not vary much throughout the domain, we

use the Beris-Edwards model as the simulations are more stable than with the Ericksen-Leslie one.

A relevant dimensionless number that characterizes the flow is the Ericksen number:

$$Er = \frac{U\ell\eta}{L}, \tag{10}$$

which gives the ratio of the viscous and the elastic forces. Here U is the characteristic velocity (e.g., the average velocity), ℓ is the characteristic length (e.g., the pitch), η is the absolute viscosity and L is the elastic constant. For instance, for sample 1 in the simulations, the corresponding Ericksen number is $Er = 1040$, which is the largest we considered, while $Er = 104$ for sample 4 in the same figure.

B. Numerics

As discussed in Ref. [41], the timescales for changes in the director and the velocity fields differ by six orders of magnitude, rendering the simulations challenging. The simulations reported in Ref. [41] use finite differences for both fields (n_α and u_α) and an adaptive time step to speed up the convergence of the velocity field. The dynamics of the director field was described by the Ericksen-Leslie theory. It was also assumed that the fluid relaxes instantaneously when compared to the director field. Here, we use the Beris-Edwards equation for the dynamics of the director field, which is solved using finite differences (predictor-corrector algorithm) while the lattice Boltzmann method is used for the velocity field. This approach results in slower but more reliable simulations, since the dynamics of the two fields are solved with the same time step. In addition, the lattice Boltzmann method is conservative while the method based on finite differences is not. Perhaps the major advantage of this approach is that the simulations are stable for parameters close to the experimental ones, which was not the case for the Ericksen-Leslie theory [41].

Due to the different timescales, which require long simulations, a compromise between the domain size and the simulation time is required. We used 2D simulation boxes, which provide useful insights into the dynamics of skyrmions in feasible simulation times. However, a 2D domain assumes invariance in the direction perpendicular to the plane, which may be a strong approximation for the velocity field. In addition, the skyrmion structure in the experiments is not invariant in the direction perpendicular to the plane. Thus, quantitative differences between the simulations and the experiments are inevitable although the qualitative behavior is expected to be captured. For instance, the flow velocities in the simulations of stable skyrmions can be much higher than those in the experiments, as shear flows in 2D are rather weak by comparison to 3D where these strong flows destroy the skyrmions.

The parameters used in the simulations are provided in Table S1 (see Supplemental Material [49]) both in simulation and physical units. We assume the material parameters of 5CB at room temperature [29,50,51]. Some of these were converted from the parameters of the Ericksen-Leslie theory to the Beris-Edwards one using the expressions given in Ref. [52] and the equilibrium nematic order parameter $S_N = 0.65$ (corresponding to the selected values of a, b and c).

For this set of parameters, corresponding to the experimental parameters of 5CB, the simulations remain stable at the cost of choosing a very small time step. The simulation domain is $L_X \times L_Y = 112 \times 56$ ($70 \times 35 \,\mu m^2$) for the simulations of a single skyrmion and $L_X \times L_Y = 200 \times 200$ ($125 \times 125 \,\mu m^2$) for the simulations of 30 skyrmions, with periodic boundary conditions in both directions. Although our simulations are in 2D, we consider $L_z = 10 \,\mu m$ when calculating the friction coefficient χ.

The initial configuration of each baby skyrmion is set as in Ref. [41] using an Ansatz for the director field:

$$
\begin{aligned}
n_x &= \sin(\tilde{a})\sin(m\tilde{b}+g), \\
n_y &= \sin(\tilde{a})\cos(m\tilde{b}+g), \\
n_z &= -\cos(\tilde{a}),
\end{aligned}
\tag{11}
$$

where

$$\tilde{a} = \frac{\pi}{2}\left[1 - \tanh\left(\frac{B}{2}(\rho - R)\right)\right], \tag{12}$$

$$\tilde{b} = \tan^{-1}\left(\frac{x - C_x}{y - C_y}\right), \tag{13}$$

$$\rho = \sqrt{(x - C_x)^2 + (y - C_y)^2}. \tag{14}$$

The parameter R controls the size of the skyrmion, B controls the width of the interface that separates the inner and the outer regions, m is the winding number of the skyrmion, g controls the direction of the skyrmion, r measures the distance from the skyrmion center, and $\tilde{b}$ is the polar angle. We set the values of these parameters (in simulation units): $m = 1$, $g = \pi/2$, $R = 0.7p$, $B = 0.5$, $C_x = L_X/2$, $C_y = L_Y/2$. The velocity field is set to zero while the Ansatz is relaxed until it reaches the steady state.

C. Frank-Oseen free energy for quasistatic analysis

We adopt the Frank-Oseen free energy to study the 3D director structures of elongated skyrmions. For chiral nematic LCs, the free energy can be expressed as

$$
\begin{aligned}
F_{FO} = \int d^3r &\left(\frac{K_{11}}{2}(\nabla \cdot \boldsymbol{n})^2 + \frac{K_{22}}{2}\left(\boldsymbol{n} \cdot \nabla \times \boldsymbol{n} + \frac{2\pi}{p}\right)^2 \right. \\
&\left. + \frac{K_{33}}{2}(\boldsymbol{n} \times \nabla \times \boldsymbol{n})^2 - \frac{\varepsilon_0\Delta\varepsilon}{2}(\boldsymbol{E} \cdot \boldsymbol{n})^2 \right),
\end{aligned}
\tag{15}
$$

where the Frank elastic constant K_{11}, K_{22}, and K_{33} determine the energy cost of splay, twist, and bend deformations, respectively. The electric field $\boldsymbol{E}$ is along z axis ($\|\boldsymbol{E}\| = U/d$, with U_E being the voltage across the cell and d the cell thickness), ε_0 is the vacuum permittivity, and $\Delta\varepsilon$ is the dielectric anisotropy of the LC. Torons emerge as local or global minima of F_{FO}, and a relaxation routine based on the variational method is used to identify energy-minimizing configurations. To obtain elongated skyrmions, we construct initial configurations by stretching the structure via lateral displacement of point defects of the toron and let the structure relax. The 3D computations are performed on $40 \times 100 \times 40$ square grids with periodic boundary conditions in the x and y directions and with fixed boundary conditions at

the bounding surfaces along the z direction. For all calculations, the following values of the model parameters are used: $d/p = 1.5$, $K_{11} = 6.4 \times 10^{-12} N$, $K_{22} = 3 \times 10^{-12} N$, $K_{33} = 10^{-12} N$, $U_E = 0.85 V$, and $\Delta\varepsilon = 13.8$.

D. Simulated polarized optical microscopy images

The polarized optical microscopy (POM) image is simulated by the Jones-matrix method, using the energy-minimizing configurations of $\boldsymbol{n(r)}$. The cell is split into 40 thin sublayers along the z direction, then we calculate the Jones matrix for each pixel in each sublayer by identifying the local optical axis and ordinary and extraordinary phase retardation. The phase retardation arises from the optical anisotropy of LC ($n_o = 1.58$ and $n_e = 1.77$ for 5CB), where the optical axis is aligned with the local molecular direction. The Jones matrix for the whole LC cell is obtained by multiplying all Jones matrices corresponding to each sublayer. We obtain the single-wavelength POM by the respective component of the product of the Jones matrix and the incident polarization. To properly reproduce the experiment POMs, we produced images separately for three different wavelengths spanning the entire visible spectrum (450, 550, and 650 nm) and then superimposed them, according to light source intensities at the corresponding wavelengths.

E. Sample preparation and experimental methods

Chiral LCs are prepared by mixing 4-cyano-4′-pentylbiphenyl (5CB, EM Chemicals) with a left-handed chiral additive, cholesterol pelargonate (Sigma-Aldrich). To define the pitch (p) of the ensuing chiral LCs, the weight fraction of the added chiral dopant is calculated using $C_{\text{dopant}} = 1/(h_{\text{htp}})$, where the helical twisting power $h_{\text{htp}} = 6.25\ \mu\text{m}^{-1}$ for the cholesterol pelargonate additive.

The sample cells are assembled from indium-tin-oxide (ITO)-coated glass slides treated with polyimide SE5661 (Nissan Chemicals) to obtain strong perpendicular (homeotropic) boundary conditions. The polyimide is applied to the surfaces by spin-coating at 2700 rpm for 30 s followed by baking (5 min at 90°C and then 1 h at 180°C).

The LC cell gap thickness is defined by silica spheres as spacers between two surfaces to be 7 μm with the cell gap to pitch ratio $d/p = 1.25$. The lateral sides of the LC cell are sealed by epoxy except for the two entrances. We use a homemade connection obtained by 3D-printing with the Formlabs Form 2 resin 3D printer (purchased from Formlab) to connect one entrance and tube, the other end of the tube being connected to a syringe. Then by pushing or pulling the plunger, the LC inside the cell channel is driven forwards or backwards. Metal wires were attached to ITO and connected to an external voltage supply (GFG-8216A, GW Instek) for electric control.

We utilize a ytterbium-doped fibre laser (YLR-10-1064, IPG Photonics, operating at 1064 nm) to generate torons. We use a sinusoidal electric field with frequency 1000 Hz to stabilize torons, which for the considered pitch over thickness ratio would, in zero field, prefer to elongate and assume finger-like structures, as discussed in section III E. Initially, we adjust the voltage across the cell to $U_E \approx 3.5$ V when the LC is uniform

and unwound. Then we melt the LC locally using a laser power around 30 mW and switch off the laser tweezers, with torons being spontaneously generated after the LC quenches back. As we drive the LC flow forwards or backwards, the torons are advected by the flow.

Polarizing optical microscopy images are obtained with a multi-modal imaging setup built around an IX-81 Olympus inverted microscope and charge-coupled device cameras (Grasshopper, Point Grey Research). Olympus objectives 20x and 10x with numerical aperture NA = 0.4 and 0.1 are used. The speed, length, and trajectories of the torons are analysed by using ImageJ (freeware from NIH).

F. Three-dimensional nonlinear optical imaging

Three-dimensional nonlinear optical imaging of elongated skyrmionic structures is performed using the three-photon excitation fluorescence polarizing microscopy (3PEF-PM) setup built around the IX-81 Olympus inverted optical microscope integrated with the ytterbium-doped fibre laser [53]. We use a Ti-Sapphire oscillator (Chameleon Ultra II; Coherent) operating at 870 nm with 140 fs pulses at an 80 MHz repetition rate as the source of the laser excitation light. An oil-immersion $40\times$ objective (NA $= 0.75$) is used to collect the fluorescence signal. The fluorescence signal is detected by a photomultiplier tube (H5784-20, Hamamatsu) after a 417/60 nm bandpass filter. The 3PEF-PM imaging involves a third-order nonlinear process, during which LC molecules are excited via the three-photon absorption process and the signal intensity scales as $\propto \cos^6(\beta)$, where β is the angle between the polarization of the excitation light and the long axis (transition dipole) of the LC molecule.

III. RESULTS

A. Flow-induced elongation of isolated skyrmions: Numerics

We start by describing the elongation of a single skyrmion due to the externally imposed material flow. In the simulations, the flow is driven by an external constant force density field. The flow field rapidly reaches a uniform steady state, due to the friction at the surfaces, which enables an accurate description of the skyrmion behavior under controlled conditions. Figure 1 illustrates the director field for the stretched skyrmion. Although the Q-tensor theory considers the symmetry between **n** and $-\mathbf{n}$, we vectorize the director field by choosing a given orientation for the director at the origin and ordering the neighboring directors only allowing smooth gradients.

Figures 2(a)–2(f) depict the time evolution of the shape of a single flow-driven skyrmion obtained at an average flow velocity $\langle u \rangle = 4636.15\ \mu\text{m/s}$ ($t_{\text{ch}} \approx 0.002$ s). Starting from a circular shape, Fig. 2(a), the skyrmion becomes axisymmetric with a small tail-like wake, Fig. 2(c), and undergoes continuous elongation in the flow direction (from the top to the bottom of the panel) beyond a characteristic time $t_{\text{ch}} = p/\langle u \rangle$. t_{ch} is the time taken by the skyrmion to move by one cholesteric pitch, which is roughly the skyrmion size at $t = 0$. The skyrmion elongation regime is illustrated in Figs. 2(d)–2(f), where the configurations are calculated at $t = 100t_{\text{ch}}$, $300t_{\text{ch}}$, $500t_{\text{ch}}$, respectively.
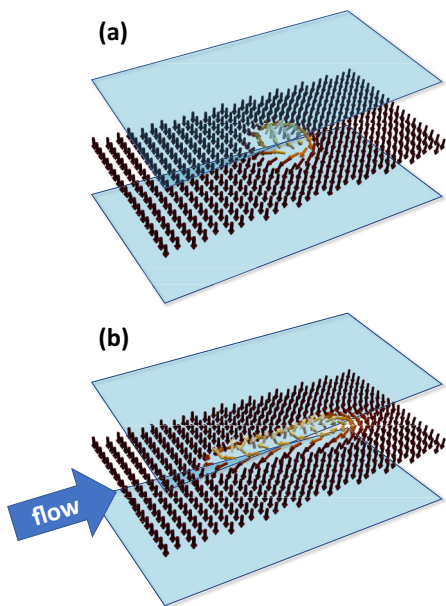
FIG. 1. (a) Initial configuration of the director field. (b) Elongated skyrmion as a result of the externally applied mass flow. The arrows represent the director field while the colours stand for its z-component (black for $n_z = -1$ and yellow for $n_z = 1$).
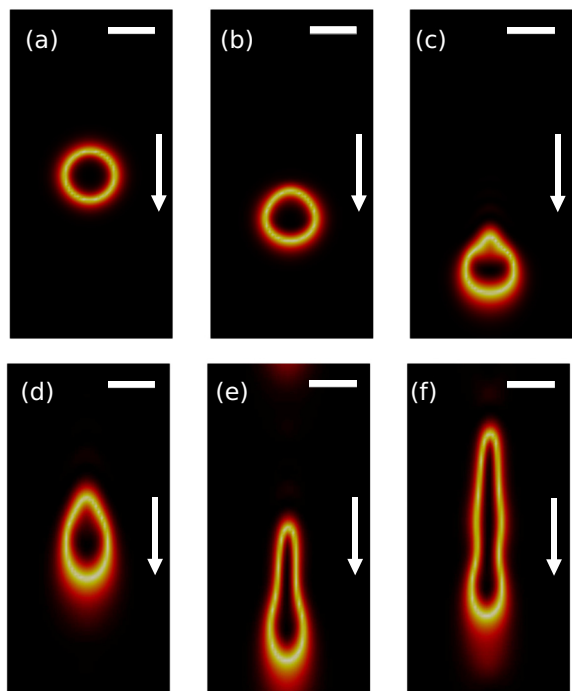

FIG. 2. Skyrmion configurations represented by color coded $|n_z|$ at $\langle u \rangle = 4636.15 \, \mu m/s$ (sample 2) at different times: (a) $t = 0$, (b) $t = 0.002$ s ($t \approx t_{ch}$), (c) $t = 0.02$ s ($t \approx 10t_{ch}$), (d) $t = 0.2$ s ($t \approx 100t_{ch}$), (e) $t = 0.6$ s ($t \approx 300t_{ch}$), and (f) $t = 1$ s ($t \approx 500t_{ch}$). Black corresponds to $|n_z| = 1$ and yellow to $|n_z| = 0$. The flow field is directed from the top to the bottom of the panels as is indicated by the white arrows. The scale bars correspond to one cholesteric pitch p.
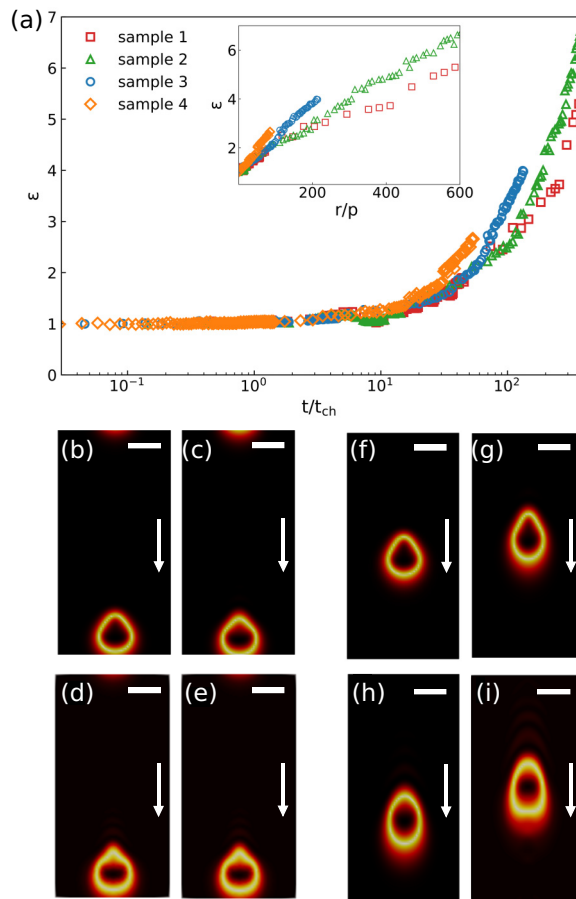

FIG. 3. (a) Aspect ratio (length/width) of the flowing skyrmions as a function of the reduced time. Different symbols correspond to different values of the average flow velocity: sample 1 with $\langle u \rangle = 14671.36 \, \mu m/s$ ($t_{ch} \approx 0.0007$ s), sample 2 with $\langle u \rangle = 4636.15 \, \mu m/s$ ($t_{ch} \approx 0.002$ s), sample 3 with $\langle u \rangle = 1467.14 \, \mu m/s$ ($t_{ch} \approx 0.007$ s), and sample 4 with $\langle u \rangle = 463.62 \, \mu m/s$ ($t_{ch} \approx 0.02$ s). The time is scaled by the characteristic time $t_{ch} = p/\langle u \rangle$. The inset illustrates the aspect ratio as a function of the total displacement divided by the pitch. (b)–(e) Skyrmion configurations obtained at $t \approx 10t_{ch}$ for different values of the average flow velocity: (b) sample 4, (c) sample 3, (d) sample 2, (e) sample 1. (f)–(i) Skyrmion configurations obtained at $t \approx 50t_{ch}$ for (f) sample 4; (g) sample 3; (h) sample 2; (i) sample 1. The flow field is directed from the top to the bottom of the panels as is indicated by the white arrows. The scale bars correspond to one cholesteric pitch p.

In Fig. 3(a), we plot the time evolution of the skyrmion aspect ratio or elongation ε, defined as the ratio of its length (parallel to the flow) and its width (perpendicular to the flow). We define the boundary of the skyrmion as the set of points where $|n_z| = 0.5$. The four curves in Fig. 3(a), corresponding to different flow velocities $\langle u \rangle$, collapse (approximately) onto a master curve when plotted against t/t_{ch}. The data collapse is better at short times $t \lesssim 10t_{ch}$, which indicates that t_{ch} is the relevant timescale in this regime. The circular skyrmion shape starts to distort at $t \gtrsim 2t_{ch}$ (see Fig 2(b), and configuration 2 in Supplemental Figs. S1–S4 [49]). Significant elongations, with $\varepsilon > 1.5$, are observed at $t \gtrsim 20t_{ch}$ for the lowest $\langle u \rangle$ [orange diamonds in Fig. 3(a)], and at $t \gtrsim 40t_{ch}$ for the other velocities

[blue circles, green triangles, and red squares in Fig. 3(a)]. At intermediate times of the order of $100t_{ch}$ the skyrmion evolves into a commet-like shape as shown in Fig 2(e), configuration 7 in Fig. S1 [49], and configuration 6 in Figs. S2–S4 [49], where $\varepsilon > 2$. Finally, at late times, we find, pearly stringlike shapes as shown in Fig 2(f), configuration 8 in Fig. S1, and configuration 7 in Figs. S2 and S3 [49]. This highlights the complex nonmonotonic dynamics of the skyrmion distortions.

We observe that at $t \gtrsim 30t_{ch}$ when $\varepsilon \gtrsim 2.0$ [compare the orange diamonds with the other symbols in Fig. 3(a)] the scaling of the elongation ε starts to break down. In particular, the data for sample 4 (orange diamonds) shifts systematically upwards relative to the master curve, i.e., the skyrmion elongation proceeds at a higher rate when $t \gtrsim 30t_{ch}$. Sample 3 follows the master curve until $t \approx 70t_{ch}$ when $\varepsilon \approx 2.3$, and then shifts upwards similarly to the previous case. Finally, at $t \gtrsim 150t_{ch}$, when $\varepsilon \approx 3.0$, the data for sample 2 (green triangles) departs from the data for sample 1. This cascade of thresholds where the scaling behavior of the elongation break down can be related to skyrmion shape changes as illustrated in Supplemental Figs. S5(a)–S5(c) [49], for samples 4-to-2 at times $t = 30, 70$, and $150t_{ch}$, respectively. All the configurations have a thin tail-like region on the left (Figs. S5(a)–S5(c) [49]), which after forming lags behind the head-like front on the right, leading to effectively faster skyrmion elongations. For comparison, we also show in Supplemental Fig. S5(d) [49] the configuration for sample 1 at $t = 150t_{ch}$ which lacks a well-defined tail-like feature. As a result, this configuration elongates more slowly.

With the aim of comparing the simulation results with experiments we depict in the inset of Fig. 3(a) the aspect ratio ε as a function of the skyrmion displacement r. The latter is defined as the distance between the skyrmion's center of mass at a given time and its initial position. We recall, that the simulations stop for all samples at the same absolute time, corresponding to different reduced times and maximal skyrmion displacements. The curves exhibit a quasilinear behavior and good data collapse is observed for $r \lesssim 10p$, in line with the scaling of $\varepsilon(t/t_{ch})$ discussed above.

The linear behavior is clear at low velocities $\langle u \rangle$, or large characteristic times (same pitch), see the orange diamonds in the inset of Fig. 3(a). At higher velocities, we find $\varepsilon \approx 1 + 0.009r/p$ for sample 2 (green triangles). The breakdown of scaling of the elongation at $r \gtrsim 10p$ ($t \gtrsim 10t_{ch}$), and the observation that in this regime ε grows faster at lower $\langle u \rangle$ [compare the orange diamonds with the red squares in Fig. 3(a)] are related to differences in the director field configurations at a given t/t_{ch} for different flow velocities $\langle u \rangle$.

Figures 3(b)–3(e) depict the skyrmion configurations under different flow velocities $\langle u \rangle$ at $t \approx 10t_{ch}$, while Figs. 3(f)–3(i) depict the configurations at a later time, $t \approx 50t_{ch}$. The first four configurations exhibit similar shapes and are in the scaling regime revealed in Fig. 3(a). Significant shape changes, however, are observed at $t \approx 50t_{ch}$ as illustrated by the last four configurations in Figs. 3(f)–3(i). Thus, the slowest skyrmion [Fig. 3(f)] is already in the elongation regime, with well-pronounced head- and tail-like regions. By contrast, the fastest skyrmion [Fig. 3(i)] has a bulletlike shape with a flat head (recall that the flow direction is from top to bottom). Furthermore, the skyrmion shape becomes fuzzier as the flow

velocity $\langle u \rangle$ increases. The differences between the samples are particularly clear when we analyze the flow field $\mathbf{u}(\mathbf{r})$ shown in Supplemental Figs. S6(e)–S6(h) [49]. As the flow velocity $\langle u \rangle$ increases, the structure of $\mathbf{u}(\mathbf{r})$ becomes irregular (see a wakelike feature in the rear of the skyrmion in Supplemental Fig. S6(h) [49]), and the velocity fluctuations from the average $\mathbf{u}(\mathbf{r}) - \langle u \rangle$ also increase.

B. Dissipation rate and Landau-de Gennes free energy

We proceed to relate the dynamics of the skyrmion distortions to the energy dissipation rate as a function of time. The work done by the external force density field [the term ρf_α in Eq. (6)] is dissipated predominantly via the effective friction [the term $-\chi u_\alpha$ in Eq. (6)], which mimics the effect of the cell surfaces. The dissipation due to the friction has the form $\int_S d^2 r \chi \rho u^2$, and as we show below it varies little with time. Therefore, in what follows we discuss only the dissipation rate $D(t)$ arising from the liquid crystal flow and the director reorientation in the bulk. As we will show below, $D(t)$ sensitively probes the dynamics of the skyrmion distortions, and provides a better understanding of the failure of the scaling of the elongation $\varepsilon(t)$ at $t \gtrsim 10t_{ch}$.

First, we note that the scalar order parameter S hardly changes in the course of the simulations, and thus we use the Ericksen-Leslie theory to calculate the dissipated energy. We follow Ref. [52] to relate the parameters of the Beris-Edwards to those of the Ericksen-Leslie equations. In the Ericksen-Leslie theory the dissipated energy by a flowing liquid crystal is given by [54]

$$D = \int_S d^2 r [\alpha_1 (n_\alpha A_{\alpha\beta} n_\beta)^2 + 2\gamma_2 N_\alpha A_{\alpha\beta} n_\beta + \alpha_4 A_{\alpha\beta} A_{\alpha\beta}$$
$$+ (\alpha_5 + \alpha_6) n_\alpha A_{\alpha\beta} A_{\beta\gamma} n_\gamma + \gamma_1 N_\alpha N_\alpha], \quad (16)$$

where the α_n's are the Leslie viscosities, $\gamma_1 = \alpha_3 - \alpha_2$, $\gamma_2 = \alpha_6 - \alpha_5$, and the corotational time flux of the director is defined as $N_\alpha = \partial_t n_\alpha + u_\beta \partial_\beta n_\alpha - W_{\alpha\beta} n_\beta$. Diagonalization of the Q tensor field yields the director field up to a sign. Therefore, we carried out a standard procedure of director vectorization. The resulting vector field is continuous and can be used to calculate the dissipated energy using Eq. (16).

We verified that upon applying the constant external force density, the fluid velocity away from the skyrmion relaxes almost instantaneously, as compared to the relaxation of the director field. Next, due to the 2D nature of this problem, this constant flow field away from the skyrmion cannot perturb the director field which has $n_z = 1$ in that region of the simulation domain. Therefore, the time dependence of all the contributions to the total dissipation rate discussed below is due solely to the director dynamics in the skyrmion proximal region.

We found that the most important contribution to $D(t)$ is due to the rotational viscosity term $\gamma_1 N_\alpha N_\alpha$ in Eq. (16). Supplemental Fig. S7 [49] compares $D(t)$ with the dissipation rate $D_{1-5}(t)$ of the other five terms $\propto \alpha_1, \gamma_2, \alpha_4, (\alpha_5 + \alpha_6)$ in Eq. (16). The conclusion is that the contribution D_{1-5} is an order of magnitude smaller than the dissipation arising from the γ_1 term. In the vicinity of the skyrmions the local flow differs from $\langle u \rangle$ (see Figs. S6(e)–S6(h) [49]), which results in a weak temporal variation of the frictional dissipation rate as shown in Supplemental Fig. S8 [49]. The quantity plotted is
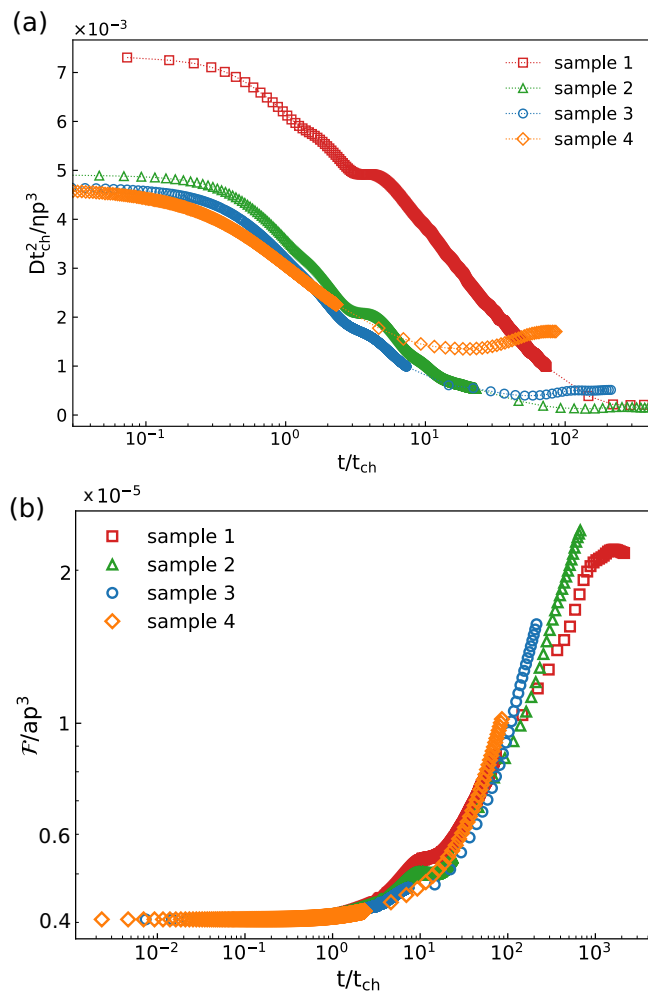
FIG. 4. (a) Dissipation rate D in Eq. (16) as a function of time; (b) Landau-de Gennes free energy as a function of time, for the flow field switched on at $t = 0$. Different symbols correspond to different values of the average flow velocity: sample 1 with $\langle u \rangle = 14671.36\,\mu m/s$ ($t_{ch} \approx 0.0007$ s), sample 2 with $\langle u \rangle = 4636.15\,\mu m/s$ ($t_{ch} \approx 0.002$ s), sample 3 with $\langle u \rangle = 1467.14\,\mu m/s$ ($t_{ch} \approx 0.007$ s), and sample 4 with $\langle u \rangle = 463.62\,\mu m/s$ ($t_{ch} \approx 0.02$ s).

the reduced frictional dissipation rate $D_f(t) = \int_S d^2 r \chi \rho (u - \langle u \rangle)^2$, defined as the excess over the frictional dissipation for a uniform flow $\langle u \rangle$. $D_f(t)$ is two orders of magnitude smaller than $D(t)$, and thus can be safely ignored.

Figure 4(a) illustrates $D(t)$ as a function of the reduced time t/t_{ch} for several values of $\langle u \rangle$. We find that the three curves corresponding to the lower values of $\langle u \rangle$ collapse approximately onto a single curve, while the curve corresponding to the largest $\langle u \rangle$ stands apart. This can be understood qualitatively by inspecting the average velocity fluctuations $\Delta \mathbf{u}(\mathbf{r}) = (\mathbf{u}(\mathbf{r}) - \langle u \rangle)$, which is at least three times larger than for the other three samples (compare the color bar in Supplemental Fig. S6(h) with those on Figs. S6(e)–S6(g) [49]). Large velocity fluctuations $|\Delta \mathbf{u}|$ enhance significantly the local velocity gradients, which in turn couple to the director field and drive it locally away from the preferred orientation. This is one of the reasons why the dissipation rate for sample 1 [red squares in Fig. 4(a)] lies

markedly above the other three curves. The regular symmetric flow pattern shows that the system is not in the turbulent regime.

Despite this difference, the curves exhibit similar qualitative behavior: (1) A short-time linear decay $\approx (C - t)$, with C a constant, for $t/t_{ch} \lesssim 1$, as shown in the Supplemental Fig. S9 [49]. (2) An intermediate time effective power-law decay $\sim t^{\alpha(t)}$, for $1 \lesssim t/t_{ch} \lesssim t^*(\langle u \rangle)$, with estimated $-5/3 \lesssim \alpha(t) \lesssim -2/3$. (3) A late-time quasiconstant regime, for $t \gtrsim t^*(\langle u \rangle)$, with $t^*/t_{ch} \approx 100, 20, 10, 2$ for samples 1 to 4, respectively. Interestingly, these values of the threshold time t^* are an order of magnitude smaller than the characteristic timescale $\gamma_1 p^2/L \approx 1.3$ s (where p is the cholesteric pitch and L is the average elastic constant) for the relaxation of the director field.

We emphasize that this separation into three regimes is only qualitative. For instance, we note a more complex behavior of $D(t)$ within regime (2) for the three highest flow velocities, where we observed short plateaulike features for $3 \gtrsim t/t_{ch} \gtrsim 5$; see Supplemental Figs. S1–S3 [49]. The emergence of such features highlights the complex skyrmion distortion dynamics even when the skyrmion shape remains almost constant at short times, see the skyrmion configurations labeled 2 and 3 in Supplemental Figs. S1–S3 [49], for example. Interestingly, this stagnation of the skyrmion elongation is accompanied by a burst in the dissipation rate due to the coupling of the flow gradients to the director field as shown in the bottom panel of Supplemental Fig. S7 [49]. This panel reveals that the dynamical regime (1) $t/t_{ch} \lesssim 1$ is also observed in the relaxation of the dissipation term D_{1-5}.

In regime (1) the dissipation rate $D(t)$ is reduced by a factor of two, while the skyrmion maintains its circular shape with $\varepsilon \approx 1$, as shown by the configuration depicted in Fig. 2(b) obtained at the end of this regime, see also the configurations labeled 1 in Supplemental Figs. S1–S4 [49]. Next, in regime (2) the total dissipation rate $D(t)$ is further reduced by approximately an order of magnitude, while the elongation is $\varepsilon \lesssim 1.5$ for samples 2, 3, and 4 as shown in Fig. 2(c) and Supplemental Fig. S2 (panel 5), Fig. S3 (panel 4), and Fig. S4 (panel 3) [49]. By contrast, for sample 1, we find a more significant skyrmion elongation at the end of regime (2), as shown in Supplemental Fig. S1 (panel 6) [49].

At late times, in regime (3) the skyrmions start to elongate and the total dissipation rate $D(t)$ takes an almost constant value (ca. 20 lower than the dissipation rate at early times). This behavior is illustrated in Supplemental Fig. S1 (panels 7, 8), Fig. S2 (panels 6, 7), Fig. S3 (panels 6, 7), and Fig. S4 (panels 5, 6) [49]. The elongation dynamics is more pronounced at the highest flow velocity (sample 1), panels 7 and 8 in Supplemental Fig. S1 [49]. The skyrmion configuration 8 extends almost throughout the whole system, reaching the limiting value of the aspect ratio. This fact is reflected by the saturation of the Landau-de Gennes free energy $F_{LdG}(t)$, as shown in Fig. 4(b) (red squares for $t \gtrsim 1000 t_{ch}$). At shorter times, $F_{LdG}(t/t_{ch})$ exhibits a linear behavior, and all the curves collapse when the time is scaled by the characteristic time t_{ch}. A closer inspection of the curves, at the three highest flow velocities, reveals the existence of plateau-like behavior at $10 \lesssim t/t_{ch} \lesssim 20$, where the skyrmion aspect ratio hardly changes, as illustrated in Supplemental Figs. S1–S3 (panels
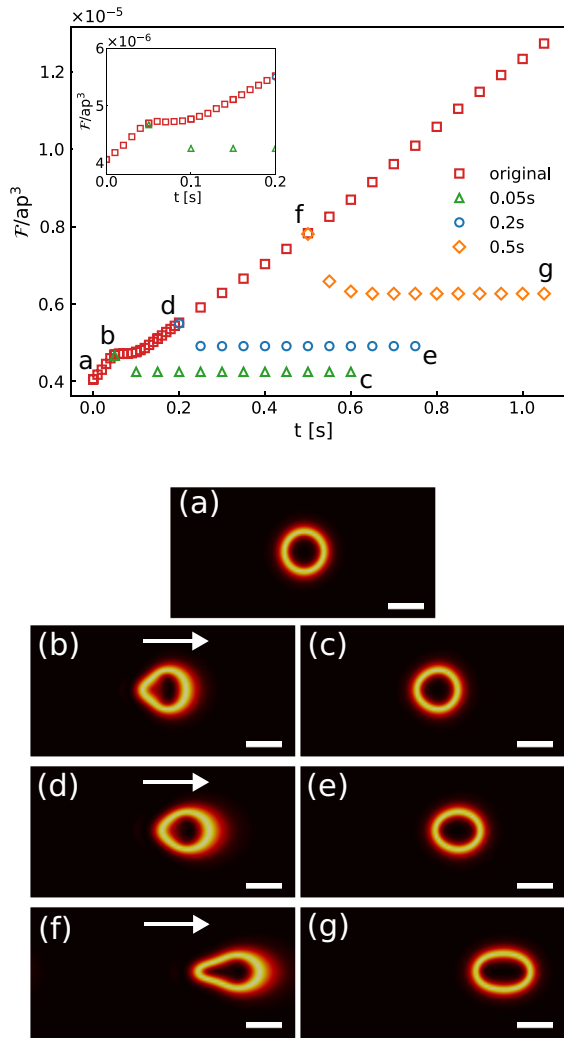
the flow is switched off, a fraction of the stored elastic free energy is dissipated, and F_{LdG} drops to a constant value, which depends on the duration of the preceding on flow cycle (see the open triangles, circles, and diamonds in Fig. 5). Somewhat unexpectedly, the free energy does not relax to its preflow value even when the flow was applied for periods as short as $7t_{ch}$, as shown by the green triangles in Fig. 5. Correspondingly, the flow-elongated skyrmions [Figs. 5(b), 5(d), and 5(f)] do not return to their original circular shape [Figs. 5(a)] and remain in distorted metastable configurations [Figs. 5(c), 5(e), and 5(g)]. This reveals that flow-induced skyrmion distortions exhibit surprising plastic behavior even at elongations as small as 10%. A natural question arises whether one can design spatio-temporal flow patterns which would result in some predefined skyrmion shape?

C. Flow-induced elongation of an isolated toron

It is challenging to control the average flow velocity in experiments due to the small size of the experimental cells. Injection of air into a cell with a syringe results in accelerated motion of the torons. Figures 6(a)–6(f) depict micrographs of toron configurations at different times as the flow proceeds through the cell, see also Supplemental video 1, which corresponds to data of sample 1 in Fig. 6(g). The toron elongation is similar to that observed in the simulations. Figure 6(g) shows the aspect ratio as a function of time for two toron realizations and flow intensities, while the inset shows the average toron velocity as a function of time. The two samples differ by the velocity of the applied flow field. As the toron velocity is not constant, the results plotted in Fig. 6(g) can not be compared directly with those in Fig. 3(a). However, by plotting the aspect ratio as a function of the toron displacement, Fig. 6(h), we observe data collapse similar to that found in the simulations [inset of Fig. 3(a)]. This observation suggests that, if the toron velocities were constant, there would be a characteristic time for which the curves for the elongation ε would collapse. It is noteworthy that even with the varying toron velocity, ε is approximately linear in displacement. For the data shown in Fig. 6(h) we find $\varepsilon \approx 1 + 0.17r/p$, where the slope is about 18 times larger than that found in simulations. We speculate that this difference may be due to the 2D approximation used in the simulations. Nevertheless, it is encouraging that even a 2D model agrees qualitatively with the experimental observations.

The plastic behavior as revealed by the results of 2D simulations (see Fig. 5) is not confirmed by the experiments. Experimentally, the torons behave elastically, i.e., after switching the flow field off, the elongated torons in the embodiment of CF2 fingers return to the original spherical shape, as demonstrated in Fig. 7 and in the Supplemental video 2. We stress, however that this observation does not preclude the existence of other experimental realizations where the plastic toron response would be possible. Indeed, we have observed that some of the stretched CF2 fingers did not fully relax to toron configurations upon turning the flow off because the dynamics and the structure of LC solitons is very sensitive to different material parameters, such as elastic anisotropy, temperature, strength of applied electric field, etc.

FIG. 5. Top: Landau-de Gennes free energy as a function of time, for the flow field switched on at $t = 0$ (red squares), and switched off at t_{off}. Triangles, circles and diamonds correspond to $t_{off} = 0.05$ s ($\approx 7t_{ch}$), 0.2 s ($\approx 29t_{ch}$) and 0.5 s ($\approx 71t_{ch}$), respectively. Data correspond to sample 3, with $\langle u \rangle = 1467.14$ μm/s. The configuration on panel (a) is at $t = 0$, and was obtained by minimizing the Landau-de Gennes free energy without flow. (b)–(g) correspond to the data labeled by the same letter on the top panel. The flow field is directed from the left to the right of the panels as is indicated by the white arrows. The scale bars correspond to one cholesteric pitch p.

4 and 5) [49]. Again, this observation emphasizes a complex nonmonotonic behavior of the skyrmion elongation dynamics, which, among others, leads to the pearly string shapes shown in Fig. 2(f).

We now proceed to discuss the reversibility of the skyrmion distortions induced by the flow. To this end, we calculate the Landau-de Gennes free energy as a function of time along two consecutive cycles when the flow field is switched on and off. Figure 5 illustrates the results for several values of the on-flow cycle. When the flow is on, after a short transient, the Landau-de Gennes free energy increases linearly with time (see open red squares in Fig. 5)—the work of the external force density is stored in the elastic distortions of the skyrmion. When
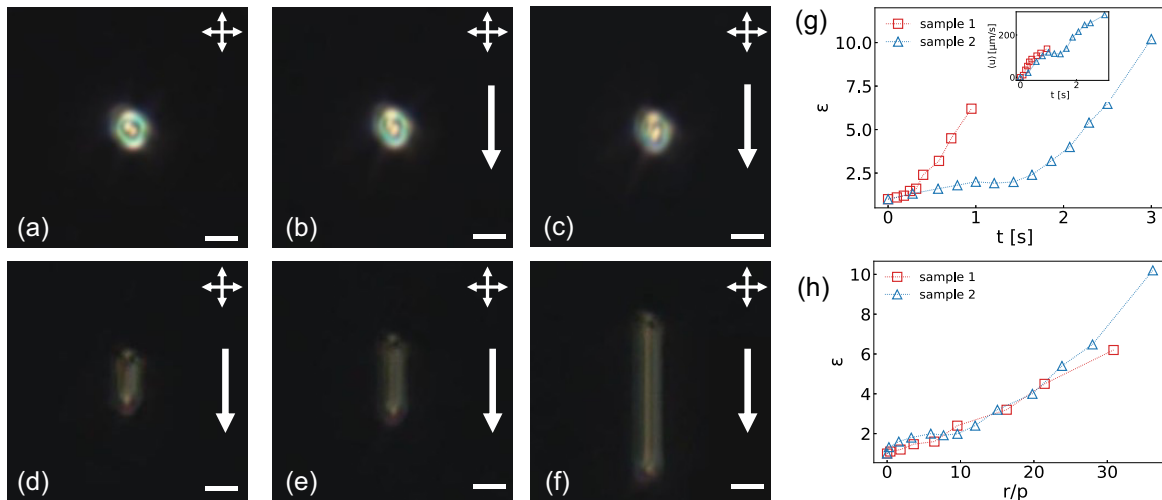
FIG. 6. (a)–(f) Show micrographs of the toron obtained at times: (a) 0 s, (b) 0.18 s, (c) 0.32 s, (d) 0.4 s, (e) 0.58 s, (f) 0.95 s. The scale bar is 10 μm and the flow is from top to bottom as indicated by the white arrows. (g) Aspect ratio and (inset) velocity against time for the two samples. (h) Aspect ratio against displacement divided by the pitch. Error bars in panels (g) and (h) are smaller than the size of the symbols. For sample 1, the toron is sped up by the flow from 0 to 135 μm/s in 0.95s, and for sample 2, the toron is sped up from 0 to 295 μm/s in 3 s.

What is the director configuration of the flow elongated torons? To answer this question we carried out a quasistatic numerical analysis of the 3D structure of the elongated torons, by minimizing the Frank-Oseen elastic free energy (see Sec. II for more technical details). Several examples of the stretched toron configurations are presented in Figs. 8(a)–8(c), using color coded director preimages, i.e., those spatial regions where the nematic director n has a given fixed value. The vectorial representations of $n(r)$, shown in Figs. 8(d) and 8(e), reveals that the topology of this extended structure remains unchanged, because the vectorized $n(r)$ taken on the (x, z) cross section of this extended configuration covers the order parameter space $\mathbb{S}^2$ once. This finding is also confirmed by directly verifying that the skyrmion number $\frac{1}{4\pi} \int n \cdot (\frac{\partial n}{\partial x} \times \frac{\partial n}{\partial z}) dx dz = 1$. The corresponding skyrmion number surface density N_{sk} in Fig. 8(f) highlights the existence of two nonsingular λ disclinations, or fractional skyrmions [55], at the top and the bottom of the cross section. In fact, this configuration is characteristic of a cholesteric finger of the second type, CF2, studied previously [13,36,56], and is often found as a metastable configuration occurring spontaneously. The

director configuration in CF2 shows how the fractional values of the skyrmion number, two half skyrmions in this case, can add up to unity in the finger, being embedded into the uniform far field background.

Figures 8(g)–8(i) compares computer-simulated and experimental POM as well as 3PEF-PM images for a system of aligned extended torons. We observe very good qualitative agreement, which demonstrates that the structure of the director field of elongated torons is identical to the structure of cholesteric fingers of the second type. More detailed numerical investigation of the torons and their interaction with the external flow is beyond the scope of this study, which will be addressed in a future work.

D. Collective effects of flowing skyrmions

When many skyrmions are subject to a flow field, their elongation may be hindered or even reversed as a result of effective interactions mediated by distortions of the LC director. In Ref. [41], two flowing skyrmions were simulated, and the resulting elongation was found to be smaller than that
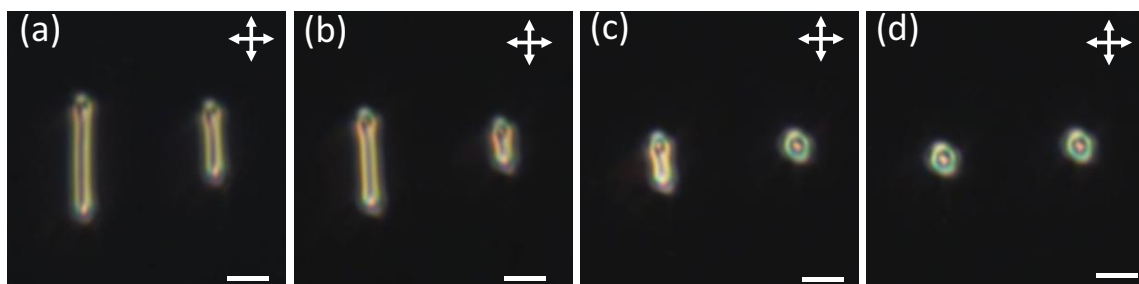

FIG. 7. Evolution of the toron elongation upon switching the external flow off. Micrographs of the toron obtained at times (a) 0 s when the flow is turned off, (b) 0.25 s, (c) 0.5 s, (d) 0.75 s when the toron returns to its original spherical shape. The scale bar is 10 μm.
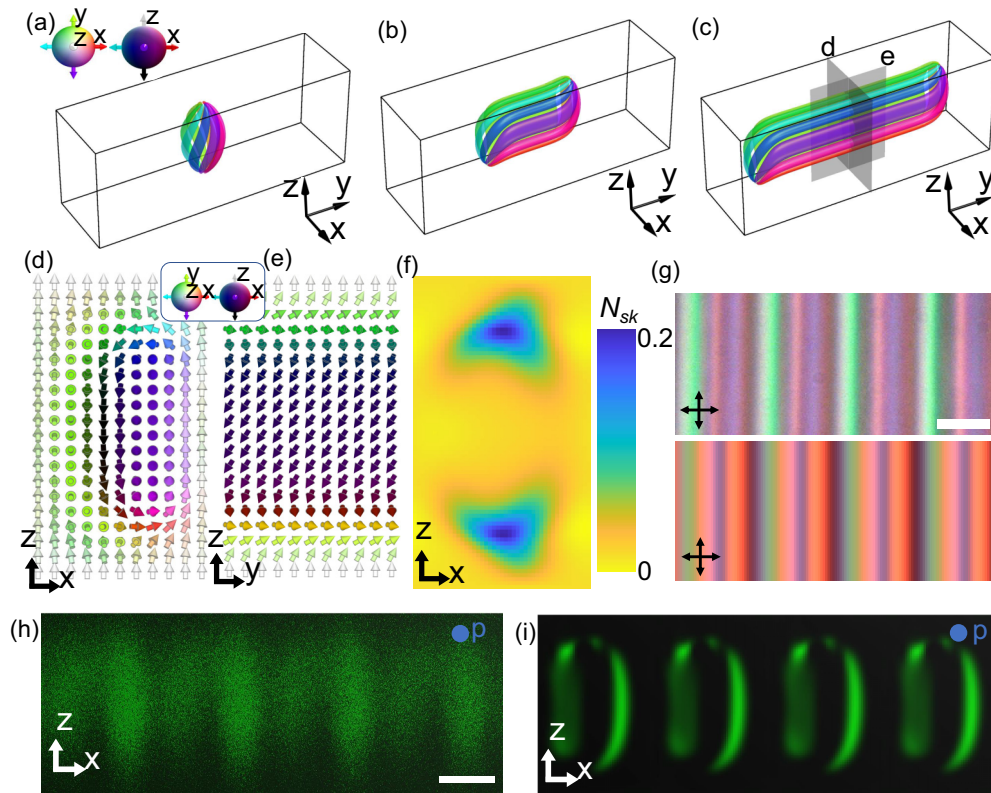
FIG. 8. (a)–(c) Preimages show the schematics of stretched torons at different elongations, where a preimage is the region in $\mathbb{R}^3$ which maps to a certain single point on the target order parameter space, the real projective plane $\mathbb{RP}^2$. The colormap is shown in the inset of panel (a). Panels (d) and (e) show detailed director fields in (x, z) and (y, z) cross-sections as marked by grey planes in panel (c). The director close to the cell surfaces is slightly tilted due to the flow drive. The colormap of different orientations of the director is shown in the inset. (f) The skyrmion number density $N_{sk} = \frac{1}{4\pi} \boldsymbol{n} \cdot (\frac{\partial \boldsymbol{n}}{\partial x} \times \frac{\partial \boldsymbol{n}}{\partial z})$ of the director field in panel (d); N_{sk} integrated over the whole cross-section in panel (d) equals unity. The color scale for N_{sk} is shown on the right. (g) Experimental (top) and computer-simulated (bottom) polarized optical micrographs of several aligned stretched skyrmions. Light propagates along the z direction. (h) Experimental and (i) computer-simulated three-photon excitation fluorescence polarizing microscopy images, where the polarization of the excitation light along the y directions is marked by p. Scale bars in panels (g) and (h) correspond to 10 μm.

of an isolated skyrmion. The skyrmion-skyrmion interaction becomes relevant at distances of the order of the cholesteric pitch.

We simulated the flow and distortions of 30 skyrmions initially placed at random on a square domain with dimensions 200×200, for an average flow velocity $\langle u \rangle = 4636.15$ μm and periodic boundary conditions. Figures 9(a)–9(d) illustrate the temporal evolution of the configuration of the ensemble of skyrmions. Most of the skyrmions elongate in the direction of the flow, with irregular transverse shape distortions due to skyrmion-skyrmion interactions. The elongation stops when the skyrmions fill the entire domain. We also observed that some skyrmions shrink as they are caged by neighboring skyrmions, as shown by the arrows in Figs. 9(a)–9(d).

We calculated the average skyrmion aspect ratio and compared it with the single skyrmion case in Fig. 9(e). Initially, the two curves evolve similarly, but at $t \approx 0.2$ s they start to deviate indicating that a skyrmion in the ensemble elongates less than an isolated skyrmion. This occurs as the interactions with neighboring skyrmions hinder the elongation of an isolated skyrmion. The error bars that increase with time indicate that the skyrmion distortions become more heterogeneous, as illustrated in Figs. 9(a)–9(d). Similar behavior was observed

in experiments with ensembles of flowing torons as shown in Figs. 9(f)–9(i) and the corresponding Supplemental video 3. The toron indicated by the arrow initially elongates and then shrinks back to an almost spherical shape as the result of interactions with the elongating neighbors.

Clearly, the elongation of flowing skyrmions discussed in the previous section occurs only if they are isolated or if their elongation proceeds along a common direction. The time dependence of the free energy of the system with 30 skyrmions is similar to that of the average aspect ratio (see Supplemental Fig. S10 [49]). At short times it is similar to that of an isolated skyrmion, flowing at the same average velocity, and it exhibits many-body effects beyond $t \approx 0.2$ s as the interactions between the elongated skyrmions become relevant. At late times the free energy increases more slowly in line with the suppression of the average elongation of the skyrmions.

E. Flow alignment of the growth directions of unstable torons

We finish by reporting an interesting experimental observation that is not reproduced by the 2D model. Under certain experimental conditions, torons have been observed to
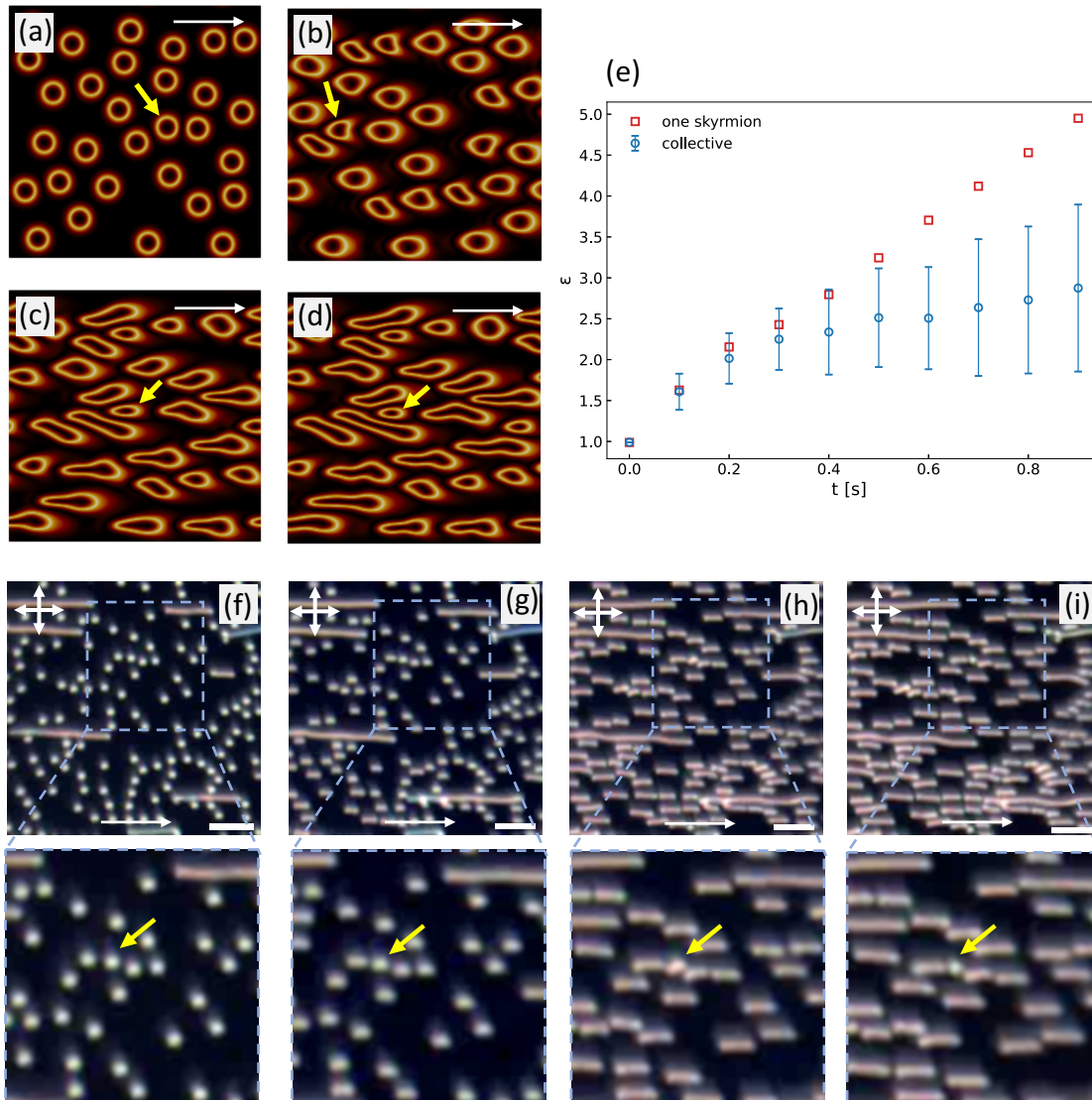
FIG. 9. (a)–(d) Time evolution of the configurations of 30 skyrmions obtained numerically at $\langle u \rangle = 4636.15$ µm. (a) 0, (b) 0.1 s, (c) 0.6 s, (d) 0.9 s. (e) Average aspect ratio as a function of time for the system with 30 flowing skyrmions depicted in panels (a)–(d). For comparison, the aspect ratio of a single skyrmion at the same flow velocity (sample 2) is also shown. The error bars represent the standard deviation of the skyrmions aspect ratio. (f)–(i) Time evolution of multiple torons in the experiments at (f) $t = 0$, (g) $t = 2$ s, (h) $t = 4$ s, and (i) $t = 6$ s. The scale bar is 50 µm and the flow is from left to right as indicated by the white arrows. The regions indicated by the squares are shown below in more detail. The yellow arrows indicate one structure (in the experiments and in the simulations) which does not elongate due to the interaction with its neighbors.

destabilize and transform into elongated CF2 fingerlike structures [56], which grow in random directions. We find that applying a flow field for a short time results in orientational ordering of the growth direction of the fingers, and the order persists when the flow is switched off.

In our experiments torons are stabilized by applying a low voltage across the cell, as shown in Fig. 10(a). When reducing the voltage, these compact structures starts to elongate in random directions, as depicted in Fig. 10(b), until filling the whole available space. Figures 10(c) shows elongating torons, but now under an applied external flow that is switched on for a short time just after the voltage reduction. We observe that it is sufficient to maintain the flow for 3 s to align all the fingers in the flow direction, as shown in Fig. 10(c). Moreover, after

switching the flow off, the orientational order persists, and the fingers continue to grow along the same direction, filling the entire space. This suggests that external flows may be effective to drive orientational ordering of cholesteric fingers. Interestingly, this ordered texture of fingers remains stable for days, although, some of the fingers shrink back to their original spherical shape under an effective compressing action of the neighboring fingers.

IV. DISCUSSION

We investigated, using experiments and numerical simulations, the distortions and the alignment of liquid crystal skyrmions under external flows for a range of average flow velocities.
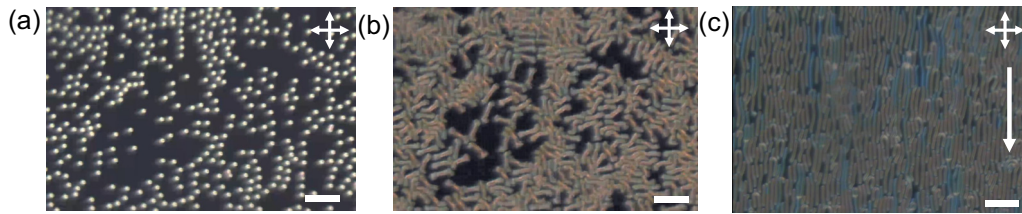
FIG. 10. In panel (a) torons are stabilized by an applied sinusoidal voltage with the amplitude of 3.5 V and the frequency 1000 Hz. In panel (b) the voltage is reduced and the torons destabilize and transform into fingers. These fingers elongate randomly and fill the entire cell. (c) Flow orients the finger growth directions. Initially, the torons are stabilized by the voltage as in panel (a), but then the voltage is reduced, and simultaneously an external flow is applied. This aligns the growing fingers along a common direction, and when the flow is turned off after 3 s of operation, the elongation proceeds in the same flow-imposed direction. The scale bars in panels (a)–(c) are 50 μm.

We performed extensive simulations based on the Landau-de Gennes Q tensor theory both for isolated as well as for systems with many skyrmions. The most striking effects were the flow-driven elongation of single skyrmions and their alignment along the flow direction in the many skyrmion system, both of which were also observed in the experiments.

The simulations were run for different flow velocities $\langle u \rangle$ and the results revealed a characteristic timescale $t_{ch} = p/\langle u \rangle$, which controls the elongation of single skyrmions, leading to data collapse or scaling of ε as a function of t/t_{ch}.

Specific features were observed depending on $\langle u \rangle$: the larger the flow velocity $\langle u \rangle$, the larger the extension of the scaling regime. This was related to a configurational transformation where the skyrmion takes a cometlike shape where the tail moves more slowly than the head. In other words the skyrmion is pulled apart by the flow, with distinct regions responding to the flow in different manners.

Furthermore, due to finite-size effects, observed at high flow velocities and long times, the free energy flattens or saturates and remains almost static as the flow induced elongation is hindered by the image skyrmion that results from the periodic boundary conditions.

We also calculated the dissipation rate and the various dissipation channels for a single skyrmion under external flows. This analysis provided insight on the observed scaling regime of the elongation of a single skyrmion and revealed a somewhat surprising plastic response at very short times. The plastic character of the skyrmion elongation occurs even at small strains, where one would expect an elastic response to the forcing. This plastic behavior is expected to be present also in the many skyrmion system and may be relevant in applications based on the alignment of soft structures such as liquid crystal skyrmions.

The experimental observations of the flow induced distortions and alignment of single and many-toron systems agree qualitatively with the numerical results, despite important differences between the model and the real system. We single out the fact that the simulations were carried out in 2D under controlled uniform flow conditions, while the experiments are in 3D and the flow was not uniform. Nevertheless, the elongation and the alignment of the distorted skyrmions by external flows appear to be robust and are qualitatively similar.

The plastic behavior uncovered by our 2D analysis was not fully confirmed by the experiments which showed reversible topology preserving toron-to-CF2 finger transformations under switching the flow on and off, even though under some conditions (Sec. III E) the torons are stretched to CF2 fingers that co-align with the flow and stay in this state after turning the flow off (differently from isolated cholesteric structures at low number densities). We emphasize, however, that the behavior of LC solitons is extremely system-dependent, and the elastic response observed here does not preclude the existence of other experimental realizations characterized by plastic behavior.

Although skyrmions are topologically 2D solitonic structures that exist as various translationally invariant (or fragments of them terminating on point singularities) field configurations within 3D chiral nematic bulk, our combined experimental and theoretical study clearly shows the pressing need of developing, on the one hand, fully 3D modeling tools to capture the full details of their behavior and, on the other hand, the coarse-grained modeling tools to model details of behavior in large multi-soliton systems under the influences of external flows, like the ones implemented here experimentally.

[1] H.-W. Chen, J.-H. Lee, B.-Y. Lin, S. Chen, and S.-T. Wu, Liquid crystal display and organic light-emitting diode display: Present status and future perspectives, Light Sci. Appl. **7**, 17168 (2018).

[2] I. I. Smalyukh, Review: Knots and other new topological effects in liquid crystals and colloids, Rep. Prog. Phys. **83**, 106601 (2020).

[3] P. E. Cladis and M. Kleman, The cholesteric domain texture, Mol. Cryst. Liq. Cryst. **16**, 1 (1972).

[4] M. Kawachi, O. Kogure, and Y. Kato, Bubble domain texture of a liquid crystal, Jpn. J. Appl. Phys. **13**, 1457 (1974).

[5] M. J. Press and A. S. Arrott, Static strain waves in cholesteric liquid crystals: Response to megnetic and electric fields, Mol. Cryst. Liq. Cryst. **37**, 81 (1976).

[6] M. J. Press and A. S. Arrott, Static strain waves in cholesteric liquid crystals. I. Homeotropic boundary conditions, J. Phys. France **37**, 387 (1976).

[7] M. J. Press and A. S. Arrott, Flow induced Grandjean lines in cholesteric liquid crystals, J. Phys. France **39**, 750 (1978).

[8] F. Lequeux, P. Oswald, and J. Bechhoefer, Influence of anisotropic elasticity on pattern formation in a cholesteric liquid crystal contained between two plates, Phys. Rev. A **40**, 3974 (1989).

[9] P. Ribière, S. Pirkl, and P. Oswald, Electric-field-induced phase transitions in frustrated cholesteric liquid crystals of negative dielectric anisotropy, Phys. Rev. A **44**, 8198 (1991).

[10] L. Gil, Numerical resolution of the cholesteric unwinding transition problem, J. Phys. II France **5**, 1819 (1995).

[11] J. Gilli, S. Thiberge, A. Vierheilig, and F. Fried, Inversion walls in homeotropic nematic and cholesteric layers, Liq. Cryst. **23**, 619 (1997).

[12] L. Gil and J. M. Gilli, Surprising Dynamics of Some Cholesteric Liquid Crystal Patterns, Phys. Rev. Lett. **80**, 5742 (1998).

[13] J. Baudry, S. Pirkl, and P. Oswald, Topological properties of singular fingers in frustrated cholesteric liquid crystals, Phys. Rev. E **57**, 3038 (1998).

[14] J. Baudry, S. Pirkl, and P. Oswald, Looped finger transformation in frustrated cholesteric liquid crystals, Phys. Rev. E **59**, 5562 (1999).

[15] P. Oswald, J. Baudry, and S. Pirkl, Static and dynamic properties of cholesteric fingers in electric field, Phys. Rep. **337**, 67 (2000).

[16] S. V. Shiyanovskii, I. I. Smalyukh, and O. D. Lavrentovich, Computer simulations and fluorescence confocal polarizing microscopy of structures in cholesteric liquid crystals, in *Defects in Liquid Crystals: Computer Simulations, Theory and Experiments*, edited by O. D. Lavrentovich, P. Pasini, C. Zannoni, and S. Žumer (Springer Netherlands, Dordrecht, 2001), pp. 229–270

[17] O. S. Tarasov, A. P. Krekhov, and L. Kramer, Dynamics of cholesteric structures in an electric field, Phys. Rev. E **68**, 031708 (2003).

[18] A. N. Bogdanov, U. K. Rößler, and A. A. Shestakov, Skyrmions in nematic liquid crystals, Phys. Rev. E **67**, 016602 (2003).

[19] P. Oswald, J. Baudry, and T. Rondepierre, Growth below and above the spinodal limit: The cholesteric-nematic front, Phys. Rev. E **70**, 041702 (2004).

[20] O. Trushkevych, P. Ackerman, W. A. Crossland, and I. I. Smalyukh, Optically generated adaptive localized structures in confined chiral liquid crystals doped with fullerene, Appl. Phys. Lett. **97**, 201906 (2010).

[21] B.-X. Li, R.-L. Xiao, S. Paladugu, S. V. Shiyanovskii, and O. D. Lavrentovich, Three-dimensional solitary waves with electrically tunable direction of propagation in nematics, Nat. Commun. **10**, 3749 (2019).

[22] L.-L. Ma, C.-Y. Li, J.-T. Pan, Y.-E. Ji, C. Jiang, R. Zheng, Z.-Y. Wang, Y. Wang, B.-X. Li, and Y.-Q. Lu, Self-assembled liquid

crystal architectures for soft matter photonics, Light Sci. Appl. **11**, 270 (2022).

[23] P. J. Ackerman, Z. Qi, Y. Lin, C. W. Twombly, M. J. Laviada, Y. Lansac, and I. I. Smalyukh, Laser-directed hierarchical assembly of liquid crystal defects and control of optical phase singularities, Sci. Rep. **2**, 414 (2012).

[24] J. S. Evans, P. J. Ackerman, D. J. Broer, J. van de Lagemaat, and I. I. Smalyukh, Optical generation, templating, and polymerization of three-dimensional arrays of liquid-crystal defects decorated by plasmonic nanoparticles, Phys. Rev. E **87**, 032503 (2013).

[25] Bryan Gin-ge Chen, P. J. Ackerman, G. P. Alexander, R. D. Kamien, and I. I. Smalyukh, Generating the Hopf Fibration Experimentally in Nematic Liquid Crystals, Phys. Rev. Lett. **110**, 237801 (2013).

[26] A. O. Leonov, I. E. Dragunov, U. K. Rößler, and A. N. Bogdanov, Theory of skyrmion states in liquid crystals, Phys. Rev. E **90**, 042502 (2014).

[27] Q. Zhang, P. J. Ackerman, Q. Liu, and I. I. Smalyukh, Ferromagnetic Switching of Knotted Vector Fields in Liquid Crystal Colloids, Phys. Rev. Lett. **115**, 097802 (2015).

[28] N. D. Mermin, The topological theory of defects in ordered media, Rev. Mod. Phys. **51**, 591 (1979).

[29] P. J. Ackerman, T. Boyle, and I. I. Smalyukh, Squirming motion of baby skyrmions in nematic fluids, Nat. Commun. **8**, 673 (2017).

[30] I. I. Smalyukh, Y. Lansac, N. A. Clark, and R. P. Trivedi, Three-dimensional structure and multistable optical switching of triple-twisted particle-like excitations in anisotropic fluids, Nat. Mater. **9**, 139 (2010).

[31] A. O. Leonov and K. Inoue, Homogeneous and heterogeneous nucleation of skyrmions in thin layers of cubic helimagnets, Phys. Rev. B **98**, 054404 (2018).

[32] G. P. Müller, F. N. Rybakov, H. Jónsson, S. Blügel, and N. S. Kiselev, Coupled quasimonopoles in chiral magnets, Phys. Rev. B **101**, 184405 (2020).

[33] P. J. Ackerman and I. I. Smalyukh, Static three-dimensional topological solitons in fluid chiral ferromagnets and colloids, Nat. Mater. **16**, 426 (2017).

[34] J.-S. B. Tai, P. J. Ackerman, and I. I. Smalyukh, Topological transformations of hopf solitons in chiral ferromagnets and liquid crystals, Proc. Natl. Acad. Sci. USA **115**, 921 (2018).

[35] C. Donnelly, K. L. Metlov, V. Scagnoli, M. Guizar-Sicairos, M. Holler, N. S. Bingham, J. Raabe, L. J. Heyderman, N. R. Cooper, and S. Gliga, Experimental observation of vortex rings in a bulk magnet, Nat. Phys. **17**, 316 (2021).

[36] H. R. O. Sohn, P. J. Ackerman, T. J. Boyle, G. H. Sheetah, B. Fornberg, and I. I. Smalyukh, Dynamics of topological solitons, knotted streamlines, and transport of cargo in liquid crystals, Phys. Rev. E **97**, 052701 (2018).

[37] A. J. Hess, G. Poy, Jung-Shen B. Tai, S. Žumer, and I. I. Smalyukh, Control of Light by Topological Solitons in Soft Chiral Birefringent Media, Phys. Rev. X **10**, 031042 (2020).

[38] J.-S. B. Tai, J.-S. Wu, and I. I. Smalyukh, Geometric transformation and three-dimensional hopping of Hopf solitons, Nat. Commun. **13**, 2986 (2022).

[39] G. Park, A. Suh, H. Zhao, C. Lee, Y.-S. Choi, I. I. Smalyukh, and D. K. Yoon, Fabrication of arrays of topological solitons in patterned chiral liquid crystals for real-time observation of morphogenesis, Adv. Mater. **34**, 2201749 (2022).

[40] H. Zhao, J.-S. B. Tai, J.-S. Wu, and I. I. Smalyukh, Liquid crystal defect structures with Möbius strip topology, Nat. Phys. **19**, 451 (2023).

[41] R. C. V. Coelho, M. Tasinkevych, and M. M. T. da Gama, Dynamics of flowing 2D skyrmions, J. Phys.: Condens. Matter **34**, 034001 (2022).

[42] P. G. de Gennes and J. Prost, *The Physics of Liquid Crystals*, International Series of Monogr (Clarendon Press, Oxford, UK, 1995).

[43] M. Doi, *Soft Matter Physics* (Oxford University Press, Oxford, UK, 2013).

[44] R. P. Trivedi, M. Tasinkevych, and I. I. Smalyukh, Nonsingular defects and self-assembly of colloidal particles in cholesteric liquid crystals, Phys. Rev. E **94**, 062703 (2016).

[45] R. C. V. Coelho, N. A. M. Araújo, and M. M. Telo da Gama, Director alignment at the nematic-isotropic interface: Elastic anisotropy and active anchoring, Philos. Trans. A: Math. Phys. Eng. Sci. **379**, 20200394 (2021).

[46] A. Duzgun, C. Nisoli, C. J. O. Reichhardt, and C. Reichhardt, Commensurate states and pattern switching via liquid crystal skyrmions trapped in a square lattice, Soft Matter **16**, 3338 (2020).

[47] Jung-Shen B. Tai and I. I. Smalyukh, Surface anchoring as a control parameter for stabilizing torons, skyrmions, twisted walls, fingers, and their hybrids in chiral nematics, Phys. Rev. E **101**, 042702 (2020).

[48] A. Beris and B. Edwards, *Thermodynamics of Flowing Systems: with Internal Microstructure*, Oxford Engineering Science Series (Oxford University Press, Oxford, UK, 1994).

[49] See Supplemental Material at http://link.aps.org/supplemental/10.1103/PhysRevResearch.5.033210 for the list of model parameters used in the simulations and an additional 10 figures to support the discussion in the main text.

[50] T. Anderson, E. Mema, L. Kondic, and L. Cummings, Transitions in Poiseuille flow of nematic liquid crystal, Int. J. Non Linear Mech. **75**, 15 (2015).

[51] P. Yeh and C. Gu, *Optics of Liquid Crystal Displays* (John Wiley & Sons, New York, NY, 2009), Vol. 67.

[52] D. Marenduzzo, E. Orlandini, M. E. Cates, and J. M. Yeomans, Steady-state hydrodynamic instabilities of active liquid crystals: Hybrid lattice Boltzmann simulations, Phys. Rev. E **76**, 031921 (2007).

[53] T. Lee, R. P. Trivedi, and I. I. Smalyukh, Multimodal nonlinear optical polarizing microscopy of long-range molecular order in liquid crystals, Opt. Lett. **35**, 3447 (2010).

[54] I. W. Stewart, *The Static and Dynamic Continuum Theory of Liquid Crystals: A Mathematical Introduction* (CRC Press, Boca Raton, FL, 2019).

[55] J.-S. Wu and I. I. Smalyukh, Hopfions, heliknotons, skyrmions, torons and both abelian and nonabelian vortices in chiral liquid crystals, Liquid Crystals Reviews, **0**, 1 (2022).

[56] I. I. Smalyukh, B. I. Senyuk, P. Palffy-Muhoray, O. D. Lavrentovich, H. Huang, E. C. Gartland, V. H. Bodnar, T. Kosa, and B. Taheri, Electric-field-induced nematic-cholesteric transition and three-dimensional director structures in homeotropic cells, Phys. Rev. E **72**, 061707 (2005).